HHS Public Access

Author manuscript

IEEE Trans Comput Imaging. Author manuscript; available in PMC 2017 December 01.

Published in final edited form as:

IEEE Trans Comput Imaging. 2016 December ; 2(4): 510–523. doi:10.1109/TCI.2016.2609414.

Spectral CT Reconstruction with Image Sparsity and Spectral Mean

Yi Zhang [Member, IEEE],
College of Computer Science, Sichuan University, Chengdu 610065, China

Yan Xi,
Department of Biomedical Engineering, Rensselaer Polytechnic Institute, Troy, NY 12180 USA

Qingsong Yang,
Department of Biomedical Engineering, Rensselaer Polytechnic Institute, Troy, NY 12180 USA

Wenxiang Cong,
Department of Biomedical Engineering, Rensselaer Polytechnic Institute, Troy, NY 12180 USA

Jiliu Zhou [Senior Member, IEEE], and
College of Computer Science, Sichuan University, Chengdu 610065, China

Ge Wang [Fellow, IEEE]
Department of Biomedical Engineering, Rensselaer Polytechnic Institute, Troy, NY 12180 USA

Abstract

Photon-counting detectors can acquire x-ray intensity data in different energy bins. The signal to noise ratio of resultant raw data in each energy bin is generally low due to the narrow bin width and quantum noise. To address this problem, here we propose an image reconstruction approach for spectral CT to simultaneously reconstructs x-ray attenuation coefficients in all the energy bins. Because the measured spectral data are highly correlated among the x-ray energy bins, the intra-image sparsity and inter-image similarity are important prior acknowledge for image reconstruction. Inspired by this observation, the total variation (TV) and spectral mean (SM) measures are combined to improve the quality of reconstructed images. For this purpose, a linear mapping function is used to minimalize image differences between energy bins. The split Bregman technique is applied to perform image reconstruction. Our numerical and experimental results show that the proposed algorithms outperform competing iterative algorithms in this context.

Index Terms

Computed tomography (CT); spectral CT; image reconstruction; total variation (TV); spectral mean (SM)

Correspondence to: Ge Wang.

Y. Zhang and Y. Xi contribute equally to this paper.

I. Introduction

DUE to its high spatial and temporal resolution, computed tomography (CT) is playing an irreplaceable role in biomedical and industrial applications [1]. However, conventional CT is based on energy-integrating detectors and yet reconstructs an attenuation coefficient distribution based on a monochromatic x-ray transmission model. The characteristic mismatch between polychromatic x-rays and energy-integrating detectors often cause loss of energy-dependent information and artifacts in a reconstructed image [2].

Recently, the research and development of spectral CT, which is also referred to as multi-energy, spectroscopic, energy-selective and energy discrimination CT, has attracted considerable interest. In the past, dual-energy CT, which can be seen as the simplest version of spectral CT, has been utilized in many applications such as material decomposition [3], automated bone removal [4] and detection of hepatocellular carcinoma and portal venography [5, 6]. Dual-energy CT can be implemented in several ways, such as dual sources, dual layer sandwich detectors, and fast kVp switching [7–9]. However, dual-energy CT still relies on the energy-integrating detectors, which integrate all of the incoming photons by the weights proportionally to their energy levels, subject to spectral blurring and beam hardening.

Different from dual-energy CT, spectral CT uses photon counting detectors (PCDs) to capture more spectrally dependent information [9]. Due to the sensitive energy discrimination and rapid photon counting, PCDs can efficiently identify a single photon and record it in a corresponding energy bin [10, 11]. Therefore, PCDs can reveal the spectral information of structures being scanned. Spectral CT has immediate and important applications, for example, low-dose CT, contrast imaging, and K-edge imaging [12–14].

For spectral CT reconstruction, a number of studies were reported. Algorithms based on the algebraic reconstruction technique (ART) perform image reconstruction by solving a system of linear equations [15], which can utilize various constraints. Statistical models are effective to handle quantum noise in a polychromatic situation [16, 17]. Some PCDs based scanners still work in the step-and-scan mode and take long data acquisition time. One solution in this situation is to reduce the number of projection views. When projection data are highly under-sampled and/or rather noisy, it would be challenging to produce a correct solution without strong prior information.

Recently, compressive sensing (CS) has been widely used in biomedical imaging [18, 19]. A critical step of CS is to choose a sparsifying transform. Valuable choices include total variation (TV) [20], wavelet [21], fast Fourier transform (FFT) [16], dictionary learning (DL) [22], and so on. As a natural application, CS was used to handle dual-energy CT and spectral CT reconstruction. Gao et al. proposed a multi-energy CT reconstruction algorithm based on the prior rank, intensity and sparsity model (PRISM) [23]. Li et al. folded images in different energy bins into a tensor form to improve the PRISM reconstruction [24]. Following the same idea, Semerci et al. presented a tensor-based nuclear norm regularization algorithm [25]. By introducing a pixel-wise penalty on the rank of the Jacobian matrix, which generalizes the gradient operator over the vector field constructed by multi-channel

images, Rigie and La Riviere proposed a joint spectral CT reconstruction model via constrained total nuclear variation (TNV) minimization [26]. In [27], a local constrained backprojection reconstruction technique [28] was adapted for spectral CT imaging, making use of correlations in the spectral domain. Although these and other methods obtained better results than the traditional analytical reconstruction, the differences and similarities were not fully considered between images in different energy bins.

In this paper, we propose a class of spectral CT reconstruction algorithms incorporating the sparsity and similarity in both the image and spectral domains [29]. The general regularization term can be expressed as

$$[\text{Sparsity within image}]+\lambda[\text{Similarity among images from different energy bins}], \quad (1)$$

where λ is a parameter to balance the two terms. To measure the similarity among images in different energy bins, we propose spectral mean (SM) to calculate the similarity patch by patch. Directly measuring the similarity between images in different energy bins will suffer from the variation of linear attenuation coefficients depending on the x-ray energy. A mapping function is constructed to improve the performance of SM by normalizing all the images in a unified fashion. With this mapping function, we formulate an objective function in a form combining data fidelity and regularization terms. Our proposed methods are different from PRISM and TNV that the similarity among images includes both edge and content. What's more, the content of each energy image is transformed by proposed linear mapping approach. The success of linear mapping applying will lead better result to spectral mean parts. Thus, linear mapping is the key of our method and the worst case of our proposed method is degraded to conventional TV-based reconstruction that only sparsity within image is considered. Here we discuss possible implementations of our reconstruction strategy. First, CT slices corresponding to different energy bins are reconstructed simultaneously. Then, TV and SM are used for two different regularization terms to capture internal sparsity and external correlations respectively.

The rest of the paper is organized as follows. In the next section, we present the details of our proposed model. In the third section, we describe experiments to evaluate the proposed methodology. In the last section, we discuss relevant issues and conclude the paper.

II. METHODOLOGY

A. Spectral CT Measurement Model

When a polychromatic x-ray beam passes through an object, the photon intensity at an energy level E measured by a photon counting detector can be formulated according to the Beer-Lambert law

$$I(E)=I_0(E)\exp\left(-\int_{\mathrm{l(x)}}\mu(\mathrm{x},\mathrm{E})dx\right) \quad (2)$$

where $\mu(x, E)$ is the linear attenuation coefficient at E and position x along the x-ray path $l(x)$, $I_0(E)$ is the intensity of incident x-rays in a spectral CT system, which can be measured by a photon counting detector in an air scan.

For current PCDs, x-ray photons are divided into several energy bins, and the number of photons in each bin is recorded. The intensity for each bin is described as

$$I(E_k)=\int_{bin(E_k)} I(E)\,dE. \tag{3}$$

where E_k denotes the energy bin which is indexed by $k \in \{1,2,\ldots, K\}$, and K is the total number of energy bins. Introducing Eq. (2) into Eq. (3), we obtain

$$I(E_k)=\int_{\mathrm{bin}(E_k)} I_0(E)\exp\left(-\int_{\mathrm{l(x)}}\mu(\mathrm{x},\mathrm{E})\mathrm{dx}\right)\mathrm{dE},k =1,2,\cdots,K. \tag{4}$$

Because the width of an energy bin is narrow with PCDs [23–26], we have the following mean value integral formula from Eq. (4),

$$I(E_k)\approx I_0(E_k)\cdot\exp\left(-\int_{\mathrm{l(x)}}\overline{\mu}(\mathrm{x},\mathrm{E_k})\,dx\right),\mathrm{k}=1,2,\cdots,\mathrm{K} \tag{5}$$

where $\overline{\mu}(x, E_k)$ is the average attenuation coefficient in the energy bin E_k, and $I(E_k)$ is the intensity of incident x-rays in the energy bin E_k. The assumption behind Eq. (5) is reasonable under the condition of a narrow energy bin width. Otherwise, a beam-hardening correction method can be applied to obtain approximate results associated with infinitesimal energy bin widths. In the experimental section, we will also validate the assumption with a polychromatic projection test. From above formula, we obtain a line integral formula at energy bin E_k

$$\int_{l(x)}\overline{\mu}(x,E_k)\,dx=\ln\frac{\mathrm{I_0(E_k)}}{\mathrm{I(E_k)}},\quad k=1,2,\cdots,K. \tag{6}$$

Eq. (6) can be discretized into a system of linear equations as follows,

$$M_k f_k=y_k,\quad k=1,2,\cdots,K \tag{7}$$

where M_k is a system matrix describing an imaging geometry, $f_k=(\overline{\mu}_{1,k},\overline{\mu}_{2,k},\cdots,\overline{\mu}_{N,k})$ is an attenuation coefficient distribution at the k-th energy bin, N is the number of image

pixels, and $y_k = \left(\ln \frac{I_0(E_k, 1)}{I(E_k, 1)}, \ln \frac{I_0(E_k, 2)}{I(E_k, 2)}, \cdots, \ln \frac{I_0(E_k, Z)}{I(E_k, Z)} \right)$ denotes projection data from intensity data measured by Z different detector elements for the k-th energy bin, $I(E_k,i)$ and $I_0(E_k,i)$ represent measured intensities with and without any object in the beam at the i-th detector position, respectively. Ideally, the system matrix should be identical for all energy bins.

Once we have Eq. (7), the purpose of the image reconstruction for spectral CT is to recover f_k from the projection data y_k, $k = 1,2,\cdots,K$. For each energy bin k, traditional analytical or iterative reconstruction algorithms can be indeed applied for spectral CT. However, due to the narrow energy bins associated with spectral CT, the photon number measured in each energy bin is much less than that with conventional energy-integrating detectors, resulting in a rather low signal to noise ratio.

B. TV-TV and TV-SM Models

Recently, CS has become popular to deal with low-dose CT reconstruction. A CS-inspired CT reconstruction model can be expressed as

$$\min_{\{f \geq 0\}} \|\Phi(f)\|_1, \ \text{s.t.} \|Mf - y\|^2 \leq \varepsilon, \quad (8)$$

wherec $\Phi(\cdot)$ is a sparsifying transform and the inequality constraint with an error tolerance factor ε is used to implement the data fidelity allowing some inconsistency in a practical situation. The symbols in the inequality constraint have the same meaning as in Eq. (7). TV is a popular sparsifying transform for image reconstruction [20, 30–35]. Also, other sparsifying transforms were also proposed [21, 22, 36].

CS-based CT image reconstruction methods are promising for spectral CT. In spectral CT, except the image sparsity itself, the similarity among images from different energy bins is also important for image reconstruction.

Fig. 1 shows typical spectral CT image reconstructions at different energy levels (The spectral CT data were acquired on a GE Discovery CT 750 HD scanner). Although the images were acquired in different energy bins, the structural information is highly correlated. Based on this observation, it is natural to utilize two different regularization terms, TV and nonlocal means (NLM). In the previous studies, TV (also called the discrete gradient transform) has shown an effect in suppressing artifacts and it has been applied for CT image reconstruction [18]. The power of TV stems from the model of image functions being piecewise constant. However, this assumption is not always valid with clinical images, which can have complex structures such as in the chest and abdominal regions. The TV regularization would blur boundaries and cause blocky effects [30, 32]. To improve the TV-based reconstruction, we will introduce a SM regularization term, which is inspired by NLM. NLM (originally developed for image denoising) has been widely used in medical imaging [37]. A major strength of NLM is that it recovers content-based information (both structural and contrast information) based on the fractal assumption of images (or images are self-similar). The system matrices M_k in our models may be different for various energy

channels due to the imaging physics of spectral CT. For coherent portions of the system matrices, artifacts cannot be eliminated by NLM. Hence, we still need a sparsity requirement such as the TV term to minimize artifacts in the prior image $\overline{f}$ from being relayed to the final image, as stated in [35]. Thus, TV and NLM are two powerful tools to address the sparsity and similarity of images simultaneously.

Based on above analysis, we give two spectral CT image reconstruction models as follows. In the first model, we use TV to incorporate the structural similarity among the images from different energy bins. The proposed model called TV-TV which is similar to the PICCS model [36, 39], and can be formulated as the following minimization problem:

$$\min_{\{f_k \geq 0\}} \delta \|f_k - \overline{f}\|_{\mathrm{TV}} + (1-\delta)\|f_k\|_{\mathrm{TV}} + \frac{\eta}{2}\|M_k f_k - y_k\|_2^2, \quad (9)$$

where $\overline{f} = J^{-1}\sum_{j=1}^{J} f_j$ is the mean of spectral images which will be dynamically updated in our algorithm, j is the index for the j-th energy bin, J is the total number of energy bins involved in the regularization (in this paper we usually set $J = K$), and $\delta \in [0,1]$ is a tuning parameter to balance two TV regularization terms. The first TV term can be seen as a constraint to couple with similar structures from different energy bins, and the second TV term is to have the sparsity inside an individual spectral image. Different from the conventional CT reconstruction, here we reconstruct images from multiple energy bins simultaneously. In [38], the authors generated the prior image using all of the data (mixed energy projection data) collected over a complete rotation. This method is designed for dual/spectral CT image reconstruction based on slow kVp switching technique. Different from this method, no predefined prior image is needed by the proposed TV-TV model. We use $\overline{f}$ as a dynamically updated prior image in the regularization term, which is more flexible and suitable for PCDs-based spectral CT image reconstruction.

The use of TV as the similarity measurement has an intrinsic high frequency differences of signals, which can be also seen as edges in 2D images, and the low frequency differences are not well captured. On the other hand, NLM is an efficient similarity measurement based on the L_2 norm focusing on both high and low frequency components. Meanwhile, NLM can take account of the similarity of adjacent pixels.

Motivated by the idea of NLM, the second model we propose is called TV-SM, and expressed as

$$\min_{\{f_k \geq 0\}} \|f_k\|_{\mathrm{TV}} + \lambda J_{\mathrm{SM}}(f_k, \overline{f}) + \frac{\alpha}{2}\|M_k f_k - y_k\|_2^2, \quad (10)$$

where $J_{\mathrm{SM}}(f_k, \overline{f})$ is the SM regularization term modified from NLM we will discuss later, λ and α are the tuning parameters. The other parameters have the same meanings as in the TV-

TV model. Similar to TV-TV, with the TV-SM method we also reconstruct images in multiple energy bins $\{f_k\}$ simultaneously.

Inspired by the prior work on the nonlocal operator [39, 40], we construct the SM regularization term $J_{\mathrm{SM}}(f_k, \overline{f})$ in the energy domain,

$$J_{\mathrm{SM}}(f_k, \overline{f}) = \sum_t w_t \| R_t f_k - R_t \overline{f} \|_2^2, \quad (11)$$

where R_t is a patch extraction operator, $t = 1,2,..., N_p$ is the index of patches, and N_p is the total number of patches. In this paper, let us use $S_P = n_p \times n_p$ to denote the patch size, and set the overlap between adjacent patches to 1. It is noted that Eq. (11) is different from the popular nonlocal means operator in [39]. Without involving any searching window, we only consider the similarity between the patches in different energy bins centered at the same location. There are two reasons for this modification. The first reason is for computational efficiency. The NLM is notorious for a high computational cost. Our algorithm simultaneously reconstructs images from different energy bins. It will be time-consuming to perform the NLM reconstruction in the original sense. The other reason is that different from 4D CT reconstruction [41], the structural similarity in spectral CT images is generally maximized at the same position across energy bins, and it will occupy most of the weights while calculating the weighting factors. As a result, it makes the search of neighboring pixels fairly insignificant. The weighting factor w_t between patches $R_t f_k$ and $R_t \overline{f}$ is defined as

$$w_t = \exp(-\mathrm{h}^{-2} \| \mathrm{R_t f_k} - \mathrm{R_t \bar{f}} \|_2^2), \quad (12)$$

where h is the parameter to control the sensitivity. The numerical schemes for TV-TV and TV-SM will be described in detail below. In our numerical schemes, w_t will be dynamically updated in each iteration as in [41].

C. Linear Mapping Function

Even if the structures in the images from different energy bins are highly correlated, the images are not completely identical. Due to the spectral dependence of linear attenuation properties, the attenuation coefficients will vary from bin to bin. This makes the images have different contrasts and HU values, as shown in Fig. 2.

The proposed TV-TV and TV-SM models can be further improved if the images from different energy bins are made more similar before the similarity computation. For this purpose, here we design a linear mapping function to minimalize these image differences between different energy bins. It will play an important pre-processing role for our TV-TV and TV-SM methods.

Let us first explain the physical principle and mathematical specifics of the linear mapping function. The purpose of this function is to adjust HU values from different energy bins into

a normalized form so that the impact of energy-dependent contrasts is minimized. Heuristically, this normalization would facilitate the regularization in both the TV-TV and TV-SM models. The physical principle of the linear mapping function is based on the material decomposition. It is well known that in a certain energy range without a K-edge, the attenuation coefficient as a function of energy can be represented as a linear combination of two base functions

$$\mu(E)/\rho \simeq a_c g_c(E) + a_p g_p(E), \quad (13)$$

where ρ is the mass density of material. a_c and a_p are material-related constants. g_c and g_p are energy dependent functions corresponding to Compton scattering and photoelectric absorption respectively [42]. Hence, measurements by two different energies through a homogeneous material of thickness L can be expressed as

$$\begin{aligned} P_h &= (a_p g_p^h + a_c g_c^h) L, \\ P_l &= (a_p g_p^l + a_c g_c^l) L. \end{aligned} \quad (14)$$

In Eq. (14), there are only two unknown variables, which can be solved uniquely to characterize the material. This is the basis for material decomposition with dual-energy CT [43], and over-determined with spectral CT.

By Eq. (14), any material ξ can be represented as a linear combination of two base materials α and β [43]:

$$\frac{\mu_\xi(E)}{\rho_\xi} = a_1 \frac{\mu_\alpha(E)}{\rho_\alpha} + a_2 \frac{\mu_\beta(E)}{\rho_\beta}, \quad (15)$$

where the linear coefficients a_1 and a_2 can be computed from physical properties of α and β.

Without loss of generality, we can use water and bone as the base materials to approximate the linear attenuation coefficients of most components in the human body with least square method in the range of 40–100 keV. The linear combination coefficients for material decomposition and root mean square errors (RMSE) are listed in Table I [43]. The data listed in Table I were calculated with the real mass attenuation coefficients of elements and mixtures from the NIST x-ray attenuation databases [44].

With Eq. (15), we let bone as the material α and water as the material β. The reason for some negative coefficients is the involved least squares fitting. Here, in the linear representation a more accurate estimation is preferred, so the coefficients in Table I are more for mathematical purpose, not based on physical consideration. If we relax the restriction of RMSE, material decomposition coefficients with physical meaning, which are within [0, 1] can be obtained. It is seen that the accuracy of linear representation is very high for the human body, as RMSE is rather close to zero. Also, an interesting phenomenon is that for most soft tissues, the main contribution is from water, and the coefficient is almost 1. It is

easy to explain that water-like liquids and soft tissues have similar linear attenuation coefficients in the range of 40–100 keV, which are very similar that of water. Based on this remark, attenuation coefficient of all the materials in the human body can be well represented in terms of a high absorption material and a low absorption material, such as water and bone. Fig. 3 shows relationships between different energy bins for the pure base materials.

In Fig. 3, all the points are located only in three positions indicated as air, water and bone. The other human tissues indicated by red crosses in Table I are all near the water. To more clearly demonstrate the relationship between any two images from different energy bins in real situations, Fig. 4 replots the HU values for the images in Fig. 1. The x coordinate denotes the HU value of one image, and the y coordinate denotes the HU value of another image in a different energy bin at the same position.

Evidently, the shapes of the curves in Fig. 4 are similar to those in Fig. 3. From Figs. 3 and 4, all of the curves indicate nonlinear relationships among different energy bins, and can be approximately seen as two linear function separated by an inflection point near 0 HU, as indicated by the red dashed line in Fig. 4. Therefore, we let the linear mapping function take the following form:

$$L_{j,k}(f_k)=\begin{cases} a^1_{j,k}f_k+b^1_{j,k}, & f_k<N_{thres} \\ a^2_{j,k}f_k+b^2_{j,k}, & f_k \geq N_{thres} \end{cases}, \quad (16)$$

where $L_{j,k}(\cdot)$ denotes the linear mapping function to transform an image f_k to f_j · $a^1_{j,k}$, $a^2_{j,k}$, $b^1_{j,k}$ and $b^2_{j,k}$ are the coefficients for the two linear functions, which can be estimated with a linear fitting method, N_{thres} indicates the singular point for the two linear functions, and is approximately equal to the HU value of water. In this paper, we set N_{thres}=0.

To estimate the coefficients of the linear mapping function, an ideal way is to use the curves in Fig. 3. However, due to the confidentiality of the calibration parameter, this method is not suitable for the images from current commercial scanner. An alternative way is to plot similar curves for the existing spectral images acquired by the same scanner. Hence, the coefficients can be calculated from these curves.

To evaluate the performance of our proposed linear mapping function, we tested it on the images in Fig. 1. We used the images in the first row of Fig. 1 to estimate the coefficients in Eq. (16). After that, we tested those coefficients on the images in the second row of Fig. 1 according to Eq. (16). The results are in Fig. 5.

In Fig. 5, the images predicted from different energy bins are quantitatively close to the original ones. The differences are not visibly noticeable. From the second and third rows of Fig. 5, the differences after linear mapping are much smaller than those from the original images. However, we can also find that the accuracy is energy-dependent, which is consistent with the visual inspection of Fig. 4. The result from 80 to 100 keV is better than that from 60 to 100 keV. A reason is that when the energy is higher, the reconstructed image

will have less noise, and the estimated linear coefficients will be more accurate. Another reason is that the 80 keV image is spectrally closer to the 100 keV image than the 60 keV image.

D. TV-TV-LM and TV-SM-LM Models

With the linear mapping Eq. (16), we immediately have the improved versions for the TV-TV and TV-SM models, which are called TV-TV-LM and TV-SM-LM respectively expressed as

$$\min_{\{f_k \geq 0\}} \left\{ \delta \| f_k - \overline{f}_k^{est} \|_{\mathrm{TV}} + (1-\delta) \| f_k \|_{\mathrm{TV}} + \frac{\eta}{2} \| M_k f_k - y_k \|_2^2 \right\}, \quad (17)$$

and

$$\min_{\{f_k \geq 0\}} \| f_k \|_{\mathrm{TV}} + \lambda J_{\mathrm{SM}}(f_k, \overline{f}_k^{est}) + \frac{\alpha}{2} \| M_k f_k - y_k \|_2^2, \quad (18)$$

where the only difference is that $\overline{f}$ is replaced by $\overline{f}_k^{est} = J^{-1} \sum_j^J L_{k,j}(f_j)$ with the other symbols being the same.

E. Split Bregman Implementation for the Proposed Models

Now, we have obtained four models for spectral CT reconstruction, which are TV-TV, TV-TV-LM, TV-SM, and TV-SM-LM respectively. For computational efficacy and numerical stability, we use the split Bregman method [40, 45] to implement our algorithms. In this section, we only describe the TV-SM-LM as an example, since the other models can be similarly implemented.

Two popular choices for the discrete TV are the isotropic TV and the L_1 -based anisotropic TV [45]. In this paper, we use an anisotropic version. First, let us give the complete discrete form of Eq. (18):

$$\min_{\{f_k \geq 0\}} |\nabla_x f_k| + |\nabla_y f_k| + \lambda J_{\mathrm{SM}}(f_k, \overline{f}_k^{est}) + \frac{\alpha}{2} \| M_k f_k - y_k \|_2^2, \quad (19)$$

To enable Bregman splitting, we introduce three auxiliary variables d_x, d_y and d_f for $\nabla_x f_k$, $\nabla_y f_k$ and $f_k - \overline{f}_k^{est}$ respectively. This yields the joint optimization can be rewritten as

$$\min_{\{f_k, d_x, d_y, d_f\}} \left\{ |d_x| + |d_y| + \lambda \sum_t w_t \| R_t d_f \| + \frac{\alpha}{2} \| M_k f_k - y_k \|_2^2 \right.$$
$$\left. + \frac{\beta}{2} \| d_x - \nabla_x f_k \|_2^2 + \frac{\beta}{2} \| d_y - \nabla_y f_k \|_2^2 + \frac{\gamma}{2} \| d_f - (f_k - \overline{f}_k^{est}) \|_2^2 \right\} \quad (20)$$

where β and γ are respectively the weights of the penalty terms. Consequently, we have the complete form of the split Bregman iteration scheme:

$$\begin{aligned}
&(f_k^{i+1}, d_x^{i+1}, d_y^{i+1}, d_f^{i+1}) \\
&=\mathrm{argmin}_{\{\mathrm{f_k},\mathrm{d_x},\mathrm{d_y},\mathrm{d_f}\}} \left\{ |\mathrm{d_x}|+|\mathrm{d_y}|+\lambda\sum_{\mathrm{t}}\mathrm{w_t}\|\mathrm{R_t d_f}\| \right. \\
&+\tfrac{\alpha}{2}\|M_k f_k - y_k\|_2^2+\tfrac{\beta}{2}\|d_x - \nabla_x f_k - b_x^i\|_2^2+ \\
&\left.\tfrac{\beta}{2}\|d_y - \nabla_y f_k - b_y^i\|_2^2+\tfrac{\gamma}{2}\|d_f - (f_k - \overline{f}_k^{est}) - b_u^i\|_2^2 \right\}, \\
&b_x^{i+1}=b_x^i+\nabla_x f_k^{i+1} - d_x^{i+1}, \\
&b_y^{i+1}=b_y^i+\nabla_y f_k^{i+1} - d_y^{i+1}, \\
&b_u^{i+1}=b_u^i+(f_k^{i+1} - \overline{f}_k^{est,i+1}) - d_y^{i+1}.
\end{aligned} \tag{21}$$

In this form, we can decouple the original problem into several sub-problems that can be solved via alternating minimization:

$$\begin{aligned}
f_k^{i+1}=&\mathrm{argmin}_{\{\mathrm{f_k}\}} \left\{ \tfrac{\alpha}{2}\|\mathrm{M_k f_k} - \mathrm{y_k}\|_2^2+\tfrac{\beta}{2}\|\mathrm{d_x^i} - \nabla_{\mathrm{x}}\mathrm{f_k} - \mathrm{b_x^i}\|_2^2 \right. \\
&\left.+\tfrac{\beta}{2}\|d_y^i - \nabla_y f_k - b_y^i\|_2^2+\tfrac{\gamma}{2}\|d_f^i - (f_k - \overline{f}_k^{est}) - b_f^i\|_2^2 \right\},
\end{aligned} \tag{22}$$

$$d_x^{i+1}=\mathrm{argmin}_{\{\mathrm{d_x}\}} \left\{ |\mathrm{d_x}|+\frac{\beta}{2}\|\mathrm{d_x} - \nabla_{\mathrm{x}}\mathrm{f_k^{i+1}} - \mathrm{b_x^i}\|_2^2 \right\}, \tag{23}$$

$$d_y^{i+1}=\mathrm{argmin}_{\{\mathrm{d_y}\}} \left\{ |\mathrm{d_y}|+\frac{\beta}{2}\|\mathrm{d_y} - \nabla_{\mathrm{y}}\mathrm{f_k^{i+1}} - \mathrm{b_y^i}\|_2^2 \right\}, \tag{24}$$

and

$$\begin{aligned}
d_f^{i+1}=&\mathrm{argmin}_{\{\mathrm{d_f}\}} \left\{ \lambda\sum_{\mathrm{t}}\mathrm{w_t}\|\mathrm{R_t d_f}\|_2^2 \right. \\
&\left.+\tfrac{\gamma}{2}\|d_f - (f_k^{i+1} - \overline{f}_k^{est,i+1}) - b_f^i\|_2^2 \right\}.
\end{aligned} \tag{25}$$

These sub-problems can be sequentially solved as

$$\begin{aligned}
f_k^{i+1}=&(\alpha M_k^T M_k - \beta\Delta+\gamma I)^{-1}(\alpha M_k^T y_k \\
&\beta(\nabla_x^T d_x^i - \nabla_x^T b_x^i+\nabla_y^T d_y^i - \nabla_y^T b_y^i)+\gamma(d_f^i+\overline{f}_k^{est,i} - b_f^i)),
\end{aligned} \tag{26}$$

$$d_x^{i+1}=\text{shirnk}(\nabla_x f_k^{i+1}+b_x^i, 1/\beta), \quad (27)$$

$$d_y^{i+1}=\text{shirnk}(\nabla_y f_k^{i+1}+b_y^i, 1/\beta), \quad (28)$$

and

$$d_f^{i+1}=\gamma\left(\alpha\sum_t w_t R_t^T R_t+\gamma I\right)^{-1}\cdot(f_k^{i+1}-\overline{f}_k^{est,i+1}+b_f^i). \quad (29)$$

where $\text{shirnk}(\kappa,\tau)=\text{sgn}(\kappa)\cdot\max(|\kappa|-\tau,0)$.

Finally, the main steps of the proposed algorithm can be summarized in Table II.

F. Experimental Data Acquisition

To evaluate the performance of the proposed approach, three datasets were used, which are numerical, ex vivo and in vivo respectively. The TV-based method for monochromic image reconstruction (TV) [20], tensor-based PRISM (tPRISM) [24], TV-TV, TV-TV-LM, TV-SM and TV-SM-LM were used for comparison. For fairness, all the algorithms were implemented using the split Bregman technique. Since the split Bregman iteration converges fast, we set the iteration number to 25. In all the experiments, we experimentally set δ=0.5, η=0.5, λ=10, α=0.5, β=100, γ=100, h=0.1, N_{outer}=25, and tol=0.001. For TV and tPRISM, the parameters were set according to the recommendation in the original papers. For the linear mapping function, in clinical data study, we used the coefficients estimated with the images of the first row of Fig. 1 and in ex vivo and in vivo, we used the coefficients estimated from identical scanner.

Image quality was assessed by two metrics that are typical. The first metric to evaluate noise reduction is the relative root mean square error (rRMSE), which is defined as

$$\text{rRMSE}=(\|f-f^*\|_2^2/\|f^*\|_2^2)^{1/2}, \quad (30)$$

where f is the reconstructed attenuation coefficient distribution, f^* is the ideal attenuation counterpart of f.

The second one is SSIM, which measures the structural and perceptual similarity between the ideal and reconstructed images:

$$\text{SSIM}=\frac{2e_f e_{f^*}(2\sigma_{ff^*}+c_2)}{(e_f^2+e_{f^*}^2+c_1)(\sigma_f^2+\sigma_{f^*}^2+c_2)}, \quad (31)$$

where e_f and e_{f^*} are the mean values of f and f^*, σ_f and σ_{f^*} are the standard deviations of f and f^* respectively, σ_{ff^*} is the covariance of them, and c_1 and c_2 are constants [46].

1) Clinical Data Study—In this study, the data were collected on a GE Discovery CT 750 HD, which is a dual-energy CT scanner using the fast kVp-switching technology. VMI images were generated using the GE commercial software at 10 keV monochromatic energy level increments from 60 to 100 keV, resulting in 5 image sets. A representative slice was specified from the image volume to evaluate our methodology. The image is of 256×256 pixels. Without loss of generality, the projection data were simulated by projecting the image into its sinogram. Siddon's ray-driven algorithm [47] in fan-beam geometry was used to simulate projections. The source-to-rotation center distance was set to 100 cm, and the detector-to-rotation center to 50 cm. The image array covered 51.2×51.2 cm^2. The detector whose length was 76.8 cm and modeled as a straight-line array of 512 elements. To demonstrate the capability of the proposed methodology for low dose reconstruction, 36 views of each energy bin were collected, and these energy bins were uniformly distributed over a full scan range.

2) Phantom Study—To validate the robustness of the assumption used in Eq. (5), we performed a phantom experiment with noisy polychromatic measurements. A modified FORBILD thorax phantom containing 256×256 pixels was generated for this experiment. The phantom consisted of seven different materials to simulate lung, heart, artery, bone, soft tissue, air, and a contrast agent composed of 0.5% gadolinium plus 99.5% water. The mass attenuation coefficients of all elements and mixtures were obtained from the NIST x-ray attenuation databases [44]. Fig. 6 plots a 110 kVp polychromatic spectrum which is generated according to the method in [48]. The spectrum is divided into 7 segments and five central parts are used in the simulation. The central energy values are 40, 50, 60, 70 and 80 keV and the widths of the energy bins are 10 keV. The spectrum resolution is 1 keV. The k-edge of the contrast agent is near 50keV. Fig. 7 is the modified thorax phantom at 50keV with material indicators and six ROIs. The lines marked by blue letters crossing the edges in different contrast levels were used for the modulation transfer function (MTF) computation to characterize the spatial resolution of the reconstructed images. The geometry is the same as that in the clinical case. The modified thorax phantom was undersampled by each energy bin with 16 views. The ideal PCD detector was assumed here and we synthesized the polychromatic measurements with the spectral weights in Fig. 6. Meanwhile, Poisson noise with $b_0 = 5 \times 10^5$ was added into each projection. Because TV directly deals with individual images, instead of reconstructing images from all energy bins simultaneously, there is no need for us to give the results of TV in this part.

3) Ex Vivo Data Study—We test our methods on an ex vivo dataset from a fresh lamb chop acquired by a MARS spectral CT scanner equipped with the latest Medipix3RX photon counting detector from University of Canterbury, Christchurch, New Zealand [49]. The scanner used a 2 mm thickness CdTe sensor (128×128 pixels, 110μm in pixel size), bump bonded to a Medipix3RX readout chip. The focal spot size was ~33μm in size. The bias voltage applied to the sensor was −440V. The source to detector distance (SDD) was 131.8mm, and the object to detector distance (ODD) was 48mm. The tube was operated at

50 kVp and 120 mA. Four low energy thresholds were used which are 15, 20, 25, and 30 keV. The exposure time was 40 ms. The original number of projection views was 651. To demonstrate the performance of our proposed approach in accelerating the scanning time, we reduced the number of views to 81, which was about 1/8 of the original number. These energy bins were uniformly distributed over a full scan range. The dataset can be publicly accessed online. More details about this dataset can be found in [49]. Dark pixel correction and projection data stitching were performed before reconstruction. Due to no post-processing operations applied, it can be seen that all the images contain some ring artifacts.

III. RESULTS

A. Clinical Data Study

1) Visual inspection—Fig. 8 displays the reconstructed 80 keV image. The images were reconstructed using TV, tPRISM, TV-TV, TV-TV-LM, TV-SM and TV-SM-LM algorithms respectively. The full-view FBP reconstruction in Fig. 1(e) serves as the reference. It is observed in Fig. 8 that there are still visibly noticeable artifacts in the TV and tPRISM images. In the other results, the artifacts are basically eliminated. To visualize the results better, Fig. 9 give a narrow window presentation demonstrating the differences of TV, tPRISM, TV-TV, TV-TV-LM, TV-SM and TV-SM-LM reconstructions relative to the reference.

As expected, TV and tPRISM had evident noise and artifacts. Although the TV-TV and TV-TV-LM algorithms eliminated more artifacts than the popular TV algorithm, some structural information was lost. In contrast, the TV-SM algorithm obtained a better reconstruction than TV-TV and TV-TV-LM, but there are still artifacts near the spine in the middle of Fig. 9(e). The TV-SM-LM algorithm achieved the best reconstruction in terms of artifact reduction and structural fidelity. Fig. 10 focuses on the zoomed parts indicated by the red box in Fig. 8.

Given the nature of TV, blocky artifacts of different degrees can be seen in the TV, tPRISM, TV-TV and TV-TV-LM images. Although in the TV-SM and TV-SM-LM images, the TV term still played a role, the inclusion of the SM term effectively suppressed the blocky problem while preventing the soft tissue edges from being blurred.

2) Quantitative measurement—To quantitatively evaluate the proposed TV-TV, TV-TV-LM, TV-SM and TV-SM-LM algorithms, the rRMSE and SSIM indices were measured for the reconstructed images, as listed in Tables III and IV.

All the algorithms that utilized information from other energy bins yielded better indices than TV in terms of either rRMSE or SSIM. In Table III, the proposed TV-SM-LM algorithm worked the best. It can be oberseved as an evidence that TV-SM-LM has a great potential to suppress artifacts caused by the lack of projection views. In Table IV, TV-SM-LM also gave the highest SSIM value except for 100keV. A possible reason for this small disturbance in SSIM is that when the energy bin is of high keV, a reconstructed image could contain less information of soft tissue, and become smoother. Nevertheless, the SSIM value at 100keV for TV-SM-LM was still comparable to the counterpart for TV-TV. This

demonstrates that the TV-SM-LM algorithm is the most competitive among all the algorithms under investigation.

3) Influence of the linear mapping function—The linear mapping function is important in our proposed methodology. We have given the quantitative results of TV-TV, TV-TV-LM, TV-SM and TV-SM-LM in Tables III and IV. It is seen that when the energy bin is lower than 80 keV, the rRMSE and SSIM indices of TV-TV-LM were better than those of TV-TV, and in most cases, the results of TV-SM-LM are better than TV-SM. The reason is that TV is only sensitive to the structural information, being not sensitive to the contrast variation between different tissues. On the other hand, SM not only preserves the structural information but also captures the contrast difference. That is also the reason why TV-SM can be improved with the linear mapping function.

4) Influence of other parameters—To evaluate the effects of the algorithmic parameters, we obtained data on the same image used in the previous experiments.

a) Size of an image patch: We studied the effect of the size of an image patch for TV-SM-LM. In this simulation, we fixed other parameters and just changed the patch size from 3×3 to 9×9. The rRMSE and SSIM values of TV-SM-LM are plotted against the patch size n_p in Fig. 11. It is seen that with the increment in the patch size, the rRMSE values initially declined, but when the patch size was greater than 7, they became saturated. Also, the SSIM curves revealed consistent results. Hence, we empirically set n_p =7 as an optimal choice. In the subsequent experiments, the optimal choice of patch size may fluctuate with the images, but we fixed it to 7 for fairness and simplicity.

b) Number of energy bins *J*: We set the patch size n_p=7 and fixed other parameters as well except for the number of energy bins *J*. The rRMSE and SSIM results at 80keV are shown in Fig. 12 with *J*=1,3,5 respectively. When *J*=3, we used images at 70, 80 and 90 keV. When *J*=5, we added 60 and 100 keV. It is seen in Fig. 12 that with the increment in the number of energy bins, both the quantitative indexes became better which are consistent with the heuristics that the more the energy bins used, the more information we have to improve the image reconstruction. This is also similar to the idea of nonlocal means that use of more image patches from different positions with similar structures will statistically improve the SNR of the averaged patches.

B. Phantom Study

1) Visual inspection—The reconstructed results on the both sides of the k-edge (40 and 50 keV) are in Fig. 13. In Fig. 13, tPRISM and TV-SM-LM clearly outperformed the other methods. The simulated sternum, artery and vertebra areas indicated by the white arrows can be seen as three reference regions. TV-SM-LM eliminated most of the artifacts due to the beam hardening and lack of projection data. In the region of contrast agent, except TV-TV and TV-TV-LM, all the other methods can achieve a satisfactory result.

2) Quantitative measurement—Tables V and VI show the values of rRMSE and SSIM for five energy bins.

It can be seen that the quantitative results have a similar trend with visual inspection. tPRISM achieved the best rRMSE performance, but the results of TV-SM-LM came very close. Meanwhile, TV-SM-LM had the highest SSIM values, which can be regarded as an evidence for structure preservation.

Table VII demonstrates the statistical analysis of variances for the ROIs. The results from FBP is regarded as standard reconstruction algorithm. It is obvious that TV-SM-LM significantly improved the imaging quality, and it reduced the SDs to a very small range and the mean close to the theoretical values. In most situations in Table VII, the P values are smaller than 0.05, which suggests the improvements dedicated by TV-SM-LM.

Fig. 14 demonstrates the MTFs obtained by TV-SM-LM, TV-TV-LM and tPRISM models in both high and low contrast levels from 40 and 50 keV images. It can be observed that TV-SM-LM yield a better spatial resolution than other two models in all the cases.

3) Influence of contrast agent—This simulation tested whether our methods will impact on the use of contrast agent which is also important for spectral CT. In Fig. 15, we plotted the means of linear attenuation coefficients inside a contrast agent region for different energy bins reconstructed by tPRISM, TV-TV-LM and TV-SM-LM respectively.

In Fig. 15, it is observed that two methods we proposed based on the linear mapping function can reconstruct the contrast enhanced region accurately. In all the five energy bins, the results are almost identical. The result shows that although the design of the linear mapping function is based on the fact that there are no k-edge materials in the human body in the energy range of [40 100] keV, the image quality will not be significantly affected when the amount of K-edge contrast agents is not large. The reason is that when the amount of contrast agents is small, the induced error will only have a weak influence on the accuracy of the linear mapping of the total cross section/volume. However, when the body contains a large amount of contrast agents that are spread over several regions, like in tumor perfusion studies, the accuracy of the linear mapping will be compromised, and the quantitative analysis about the relationship between the accuracy of the linear mapping and the amount of contrast agents will be performed in the future.

C. Ex vivo data

Limited by the hardware of PCDs, current spectral CT scanners based on PCDs can only scan small objects and suggests the preclinical potential of spectral CT enabled by PCDs. The purpose of this experiment is twofold. First, we can evaluate the proposed methods with a real PCD dataset; and second, we can demonstrate the potential of spectral imaging of tissue without contrast agents. In Fig. 16, the results of different methods with data at 20 and 25 keV are shown and it is clear that comparing to the other methods, TV-SM-LM had the best performance. Although some artifacts remained near the bones, it suppressed most of the artifacts, and meanwhile avoided the blurring effect like that with tPRISM and the beam hardening problem with FBP. The contrast between meat and fat is also decent with our method. These observations suggest that our method is powerful for spectral CT reconstruction PCD data.

IV. DISCUSSIONS AND CONCLUSION

In the experimental work, we evaluated our proposed methods on three datasets. Although the first dataset was not from PCD detectors, the virtual monochromic images (VMIs) can still be used as a reasonable dataset to compare spectral CT image reconstruction algorithms [50]. In this contest, the proposed four methods outperformed the TV-based monochromatic image reconstruction model, and the tensor-based PRISM model for spectral CT reconstruction. The tensor-based PRISM model also utilized the correlation among different energy bins, but the low-rank decomposition cannot always the best for clinical images. The second experiment was conducted to evaluate the image quality for CTA with our approach. The proposed linear mapping function was designed based on a piecewise linear approximation, and it is necessary to measure the impact of contrast material on our approach. The use of the linear mapping of spectral attenuation coefficients is the key idea of this paper. It is based on the assumption that each tissue type in the human body can be represented by basis materials, such as water and bone. Fortunately, most materials can be well represented in this way, as listed in Table 1. Thanks to the data fidelity term in the reconstruction formula, the k-edge or other abnormal materials will not affect the final reconstruction quality significantly, as demonstrated in the phantom experiment. The worst case is that images reconstructed using our proposed methods will degrade to those comparable to that reconstructed using the conventional TV-based method. Since there is no PCD-based clinical spectral CT scanner available to us at present, the first experiment with VMIs was used to evaluate the performance of the proposed models. VMIs can be seen as quasi-spectral CT images, with major differences in imaging physics. Hence, the third experiment with PCD data offers complementary information.

Due to the narrow widths of energy bins and the limited number of projection views, the reconstructed results from FBP were contaminated by severe artifacts and noise. The beam hardening effect was also visible in each energy bin. Although the results of tPRISM eliminated part of the artifacts, our proposed TV-SM-LM gave the best image quality.

There are several parameters in our methods. Although all the parameters were experimentally set in our experiments, there is no critical need to adjust the parameters patient by patient for the following reasons. β and γ are the parameters for the splitting method. Once they are manually chosen to obtain a good converging rate, they can be approximately treated constants for input images in the same or similar categories, which has been reported as one of the advantages of Bregman iteration [45]. N_{outer}, and tol are the parameters to control the iterations. Normally, the convergence of the Bregman iteration is fast. To guarantee the best performance, we empirically set the numbers iterations to reasonable numbers. To stop the iteration while it has reached an optimum, we use tol as an additional control of the iteration process. The regularization parameters δ, η, λ and a in Eqs. (17) and (18) should be chosen to balance the data fidelity term and the regularization terms. There are some general strategies for choosing values of these parameters [51]. However, it is difficult to define the “optimal” regularization parameters at this moment. As far as we know, most regularization parameters required by iterative reconstruction algorithms are empirically chosen. Therefore, in this paper we have set these parameters in an empirical fashion.

In all of our proposed algorithms, the images in different energy bins are iteratively and simultaneously reconstructed, and it will be time-consuming. The SM-based algorithms even calculate the similarity values based on image patches. We improved the computational efficiency in two ways. First, we have used the split Bregman technique which has been proved computationally efficient and already applied in many fields. More details can be found in [45]. Second, we proposed spectral mean term instead of NLM, and it makes the computational complexity much reduced. Except for the techniques, we mentioned above, another possible way to accelerate the computation is to use a parallel computing technique. The computation for each energy bin is independent, and can be distributed on a graphic processing unit (GPU), a computer cluster or other concurrent computation systems. In the practical cases, the system will be large. Hence, the use of the Gauss-Seidel algorithm to solve Eq. (27) will become inefficient due to the required matrix inversion. One of the possible ways to remedy this problem is to use the Krylov subspace method, such as conjugate gradient (CG), MINRES, IDR and GMRES. Some of these methods involve a series of matrix-vector, scalar-vector and vector-vector operations, which are suitable for GPU implementation. Meanwhile, our methods are patch-based, and reconstruct the images in different channels simultaneously, which can be implemented in a parallel fashion.

In conclusion, we have proposed four spectral CT image reconstruction algorithms. In addition to the use of TV to extract the image sparsity, TV and SM have been utilized to measure the similarity of component images in the energy domain. A linear mapping function has been defined to improve the similarity measurement. The results have showed the merits of our approach.

Acknowledgments

The authors thank Drs. A. Butler, P. Butler, and R. Aamir from University of Otago, Dunedin, New Zealand for valuable discussions about the raw data acquired by the MARS spectral CT scanner. The authors thank Dr. L. Li from Tsinghua University, Beijing, China, to kindly supply the code of tPRISM. The authors also thank Dr. R. Tang from Shanghai Jiaotong University, Shanghai, China, who shared the clinical data for use in this paper.

This work was supported in part by the National Natural Science Foundation of China under Grants 61302028 and 61671312, the CSC under Grants 201308510138 and in part by the National Institute of Biomedical Imaging and Bioengineering (NIBIB)/National Institutes of Health (NIH) under Grant R01 EB016977 and U01 EB017140.

Biographies

Yi Zhang (S′11–M′12) received the B.S., M.S. and Ph.D. degrees from the College of Computer Science, Sichuan University, Chengdu, China, in 2005, 2008 and 2012, respectively. From 2014–2015, he was with the Department of Biomedical Engineering,

Rensselaer Polytechnic Institute, Troy, New York, USA, as a Postdoctoral researcher. He is currently an Associate Professor with the College of Computer Science, Sichuan University, Chengdu, China. His research interests include computed tomography, compressive sensing and deep learning.

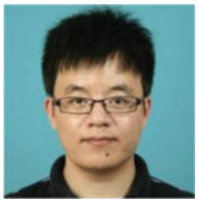

Yan Xi received the Ph.D. degree from the Department of Biomedical Engineering, Shanghai Jiao Tong University, Shanghai, China in 2013. His Ph.D. thesis was on the Applications of X-ray phase-contrast imaging in medical. His research interests include computed tomography and phase-contrast imaging.

Qingsong Yang received the B.S. degree in the Department of Engineering Physics from Tsinghua University, Beijing, China, in 2013. He is currently working towards the Ph.D. degree in biomedical engineering at Rensselaer Polytechnic Institute, Troy, New York, USA under the supervision of Prof. Ge Wang. His research interests include x-ray phase contrast imaging and photon-counting CT technology.

Wenxiang Cong received the B.S. degree in mathematics from Heilongjiang University, Harbin, China, in 1982, the M.S. degree in applied mathematics from Harbin Institute of Technology, Harbin, in 1988, and the Ph.D. degree in optical imaging from Beijing University of Science and Technology, Beijing, China, in 1998. Currently, he is a Research Scientist at the Department of Biomedical Engineering, Rensselaer Polytechnic Institute, Troy, New York, USA. His research interests include optical molecular tomographic imaging and x-ray phase contrast/dark-field tomographic imaging.

Jiliu Zhou is a Professor with the School of Computer Science and Technology, Sichuan University, Chengdu, China. Also he is the principal of Chengdu University of Information Technology, Chengdu, China. His research is mainly in the field of image processing, artificial intelligence, fractional differential application on the latest signal and image processing, and so on. He has published more than 100 papers, of which more than 80 papers are indexed by SCI, EI, or ISTP.

Ge Wang (F′03), PhD in ECE, is Clark & Crossan Endowed Chair Professor and Director of Biomedical Imaging Center/Cluster, Rensselaer Polytechnic Institute, Troy, New York, USA. His expertise includes x-ray computed tomography (CT), optical molecular tomography, multi-modality imaging, and deep learning. He wrote the pioneering papers on the first spiral cone-beam CT algorithm (1991 & 1993). He and his collaborators published the first paper on bioluminescence tomography, creating a new area of optical molecular tomography. His group published the first papers on interior tomography and omnitomography for grand fusion of all relevant tomographic modalities ("*all-in-one*") to acquire different datasets simultaneously ("*all-at-once*") with simultaneous CT-MRI as an example. His results were featured in Nature, Science, and PNAS, and recognized with various academic awards. He published over 400 journal papers, which are highly cited. He is the lead guest editor of four IEEE Trans. Medical Imaging special issues on x-ray CT, molecular imaging, compressive sensing, and spectral CT respectively, the founding Editor-in-Chief of International Journal of Biomedical Imaging, Associate Editor of IEEE Trans. Medical Imaging, IEEE Access, Medical Physics, and others. He is Fellow of IEEE, SPIE, OSA, AIMBE, AAPM, and AAAS.

References

1. Wang G, Yu H, De Man B. An outlook on x-ray CT research and development. Med Phys. 2008; 35(3):1051–1064. [PubMed: 18404940]
2. De Man B, et al. An iterative maximum-likelihood polychromatic algorithm for CT. IEEE Trans Med Imag. 2001; 20(10):999–1008.

3. Johnson TRC, et al. Material differentiation by dual energy CT: initial experience. Eur Radiol. 2007; 17(6):1510–1517. [PubMed: 17151859]
4. Graser A, et al. Dual energy CT: preliminary observations and potential clinical applications in the abdomen. Eur Radiol. 2009; 19(1):13–23. [PubMed: 18677487]
5. Lv P, et al. Spectral CT in patients with small HCC: investigation of image quality and diagnostic accuracy. Eur Radiol. 2012; 22(10):2117–2124. [PubMed: 22618521]
6. Zhao LQ, et al. Improving image quality in portal venography with spectral CT imaging. Eur J Radiol. 2012; 81(8):1677–1681. [PubMed: 21444170]
7. Zou, Y., Silver, MD. Analysis of fast kV-switching in dual energy CT using a pre-reconstruction decomposition technique. Proc SPIE 6913; Bellingham, WA. 2008. p. 6913131-12
8. Heismann, B., Schmidt, B., Flohr, T. Spectral Computed Tomography. Bellingham, DC: SPIE;
9. McCollough CH, et al. Dual- and multi-energy ct: principles, technical approaches, and clinical applications. Radiology. 2015; 276(3):637–653. [PubMed: 26302388]
10. Yang Q, et al. Spectral x-ray CT image reconstruction with a combination of energy-integrating and photon-counting detectors. PLoS One. 2016; 11(5):e0155374. [PubMed: 27171153]
11. Shikhaliev PM, Fritz SG. Photon counting spectral CT versus conventional CT: comparative evaluation for breast imaging application. Phys Med Biol. 2011; 56(7):1905–1930. [PubMed: 21364268]
12. Xu Q, et al. Image reconstruction for hybrid true-color micro CT. IEEE Trans Biomed Eng. 2012; 59(6):1711–1719. [PubMed: 22481806]
13. Meng B, et al. Energy window optimization for x-ray k-edge tomographic imaging. IEEE Trans Biomed Eng. [Online] Available: 10.1109/TBME.2015.2413816.
14. Xi Y, et al. United iterative reconstruction for spectral computed tomography. IEEE Trans Med Imag. 2014; 34(3):769–778.
15. Gordon R, Bender R, Herman GT. Algebraic reconstruction techniques (ART) for three-dimensional electron microscopy and x-ray photography. J Theor Biol. 1970; 29(3):471–481. [PubMed: 5492997]
16. Elbakri IA, Fessler JA. Statistical image reconstruction for polyenergetic x-ray computed tomography. IEEE Trans Med Imag. 2002; 21(2):89–99.
17. Schirra CO, et al. Statistical reconstruction of material decomposed data in spectral CT. IEEE Trans Med Imag. 2013; 32(7):1249–1257.
18. Candès EJ, Romberg J, Tao T. Robust uncertainty principles: Exact signal reconstruction from highly incomplete frequency information. IEEE Trans Inform Theory. 2006; 52(2):489–509.
19. Donoho DL. Compressed sensing. IEEE Trans Inform Theory. 2006; 52(4):1289–1306.
20. Sidky EY, Pan X. Image reconstruction in circular cone-beam computed tomography by constrained, total-variation minimization. Phys Med Biol. 2008; 53(17):4777–4807. [PubMed: 18701771]
21. Tang S, Tang X. Statistical CT noise reduction with multiscale decomposition and penalized weighted least squares in the projection domain. Med Phys. 2012; 39(9):5498–5512. [PubMed: 22957617]
22. Xu Q, et al. Low-dose x-ray CT reconstruction via dictionary learning. IEEE Trans Med Imag. 2012; 31(9):1682–1697.
23. Gao H, et al. Multi-energy CT based on a prior rank, intensity and sparsity model (PRISM). Inverse Probl. 2011; 27(11):115012. 1-22. [PubMed: 22223929]
24. Li L, et al. Spectral CT modeling and reconstruction with hybrid detectors in dynamic-threshold-based counting and integrating modes. IEEE Trans Med Imag. 2015; 34(3):716–728.
25. Semerci O, et al. Tensor-based formulation and nuclear norm regularization for multienergy computed tomography. IEEE Trans Image Process. 2014; 23(4):1678–1693. [PubMed: 24808339]
26. Rigie DS, La Riviere PJ. Joint reconstruction of multi-channel, spectral CT data via constrained total nuclear variation minimization. Phys Med Biol. 2015; 60(5):1741–1762. [PubMed: 25658985]
27. Leng S, et al. Noise reduction in spectral CT: reducing dose and breaking the trade-off between image noise and energy bin selection. Med Phys. 2011; 38(9):4946–4957. [PubMed: 21978039]

28. Johnson KM, et al. Improved waveform fidelity using local HYPR reconstruction (HYPR LR). Magn Reson Med. 2008; 59(3):456–462. [PubMed: 18306397]
29. Zhang, Y., et al. IEEE 12th International Symposium on Biomedical Imaging (ISBI). 2015. Spectral CT reconstruction using image sparsity and spectral correlation; p. 1600-1603.
30. Liu Y, et al. Adaptive-weighted total variation minimization for sparse data toward low-dose x-ray computed tomography image reconstruction. Phys Med Biol. 2012; 57(23):7923–7956. [PubMed: 23154621]
31. Yu H, Wang G. A soft-threshold filtering approach for reconstruction from a limited number of projections. Phys Med Biol. 2010; 55(13):3905–3916. [PubMed: 20571212]
32. Zhang Y, et al. Few-view image reconstruction with fractional-order total variation. J Opt Soc Am A. 2014; 31(5):981–995.
33. Zhang Y, et al. Statistical iterative reconstruction using adaptive fractional order regularization. Biomed Opt Express. 2016; 7(3):1015–1029. [PubMed: 27231604]
34. Zhang Y, et al. Few-view image reconstruction combining total variation and a high-order norm. Int J Imag Syst Tech. 2013; 23(3):249–255.
35. Chen G-H, Tang J, Leng S. Prior image constrained compressed sensing (PICCS): A method to accurately reconstruct dynamic CT images from highly undersampled projection data sets. Med Phys. 2008; 35(2):660–663. [PubMed: 18383687]
36. Ma J, et al. Iterative image reconstruction for cerebral perfusion CT using a pre-contrast scan induced edge-preserving prior. Phys Med Biol. 2012; 57(22):7519–7542. [PubMed: 23104003]
37. Buades A, Coll B, Morel J-M. A review of image denoising algorithms, with a new one. Multiscale Model Sim. 2005; 4(2):490–530.
38. Szczykutowicz TP, Chen G-H. Dual energy CT using slow kVp switching acquisition and prior image constrained compressed sensing. Phys Med Biol. 2010; 55(21):6411–6429. [PubMed: 20938070]
39. Gilboa G, Osher S. Nonlocal operators with applications to image processing. Multiscale Model Sim. 2009; 7(3):1005–1028.
40. Zhang X, et al. Bregmanized nonlocal regularization for deconvolution and sparse reconstruction. SIAM J Imaging Sci. 2010; 3(3):253–276.
41. Tian Z, et al. Low-dose 4DCT reconstruction via temporal nonlocal means. Med Phys. 2011; 38(3): 1359–1365. [PubMed: 21520846]
42. Alvarez RE, Macovski A. Energy-selective reconstructions in x-ray computerised tomography. Phys Med Biol. 1976; 21(5):733–744. [PubMed: 967922]
43. Lehmann LA, et al. Generalized image combinations in dual KVP digital radiography. Med Phys. 1981; 8(5):659–667. [PubMed: 7290019]
44. http://www.nist.gov/pml/data/xraycoef/index.cfm.
45. Goldstein T, Osher S. The split Bregman method for L1-regularized problems. SIAM J Imaging Sci. 2009; 2(2):323–343.
46. Wang Z, et al. Image quality assessment from error visibility to structural similarity. IEEE Trans Image Process. 2004; 13(4):600–612. [PubMed: 15376593]
47. Siddon RL. Fast calculation of the exact radiological path for a three-dimensional CT array. Med Phys. 1985; 12(2):252–255. [PubMed: 4000088]
48. Siewerdsenm J, et al. Spektr: A computational tool for x-ray spectral analysis and imaging system optimization. Med Phys. 2004; 31(11):3057–3067. [PubMed: 15587659]
49. Aamir R, et al. MARS spectral molecular imaging of lamb tissue: data collection and image analysis. J Instrum. 2014; 9(2):P02005. 1-10.
50. Zeng D, et al. Spectral CT image restoration via an average image-induced nonlocal means filter. IEEE Trans Biomed Eng. 2016; 63(5):1044–1057. [PubMed: 26353358]
51. Scherzer, O. Handbook of mathematical methods in imaging. Springer; New York; London: 2011.

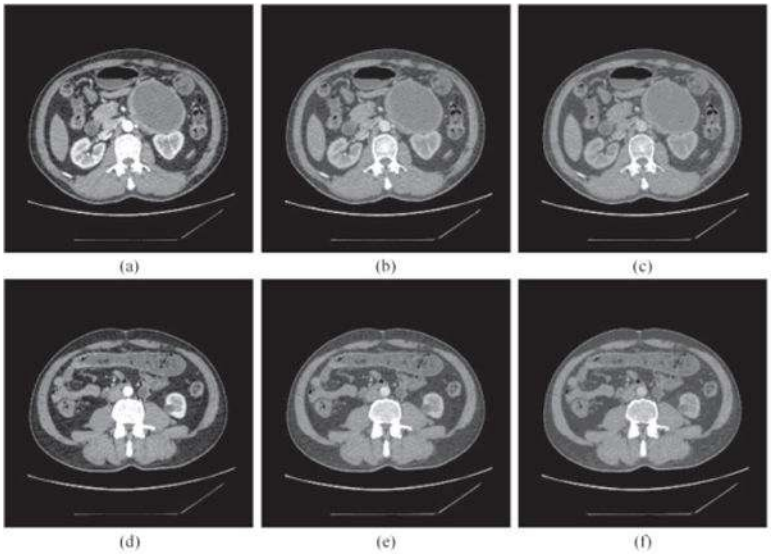

Fig. 1.

Three exemplary spectral CT image reconstructions. The first column of images was acquired at 60 keV, the second column at 80 keV, and the third column at 100 keV. The display window is [845 1295] HU.

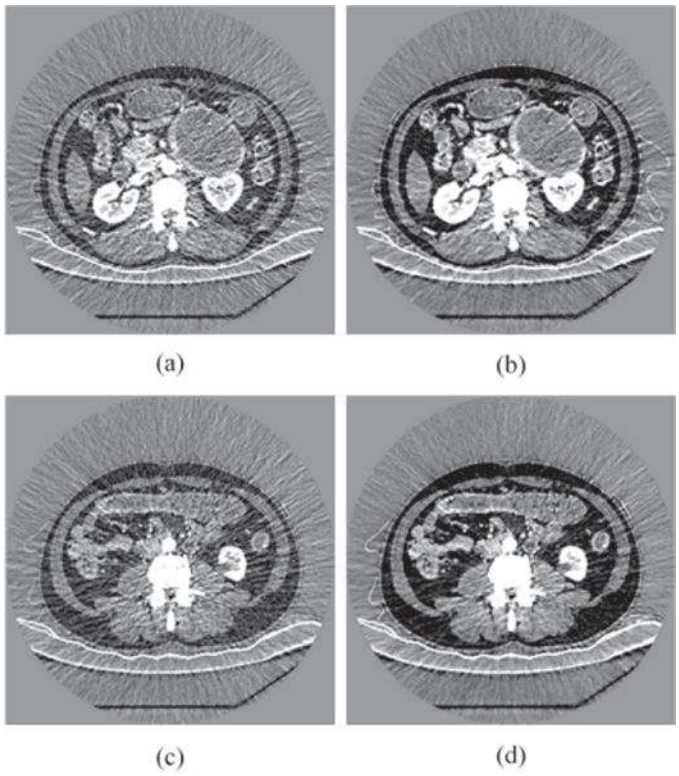

Fig. 2.

Differences between the images in Fig. 1. (a) $f_{60\text{keV}} - f_{80\text{keV}}$ for the first image example, (b) $f_{60\text{keV}} - f_{100\text{keV}}$ also for the first example, (c) $f_{60\text{keV}} - f_{80\text{keV}}$ for the second example, and (d) $f_{60\text{keV}} - f_{100\text{keV}}$ for the second example. The display window is [−50, 50] HU

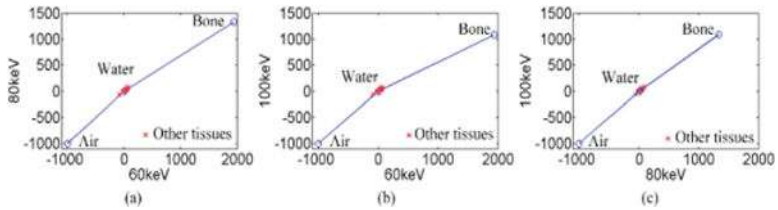

Fig. 3.

Idealized plots for main materials in the human body respectively in different energy bins. The plots for (a) x-axis 60 keV and y-axis 80 keV, (b) 60 keV and y-axis 100 keV, and (c) x-axis 80 keV and y-axis 100 keV.

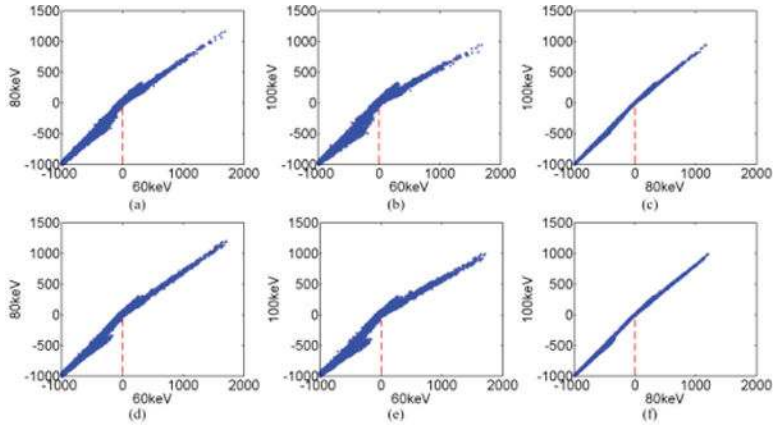

Fig. 4.

Piecewise linear relationships between two images in different energy bins. (a)–(c) The plots for the 1st image example, and (d)–(f) the plots for the 2nd image example.

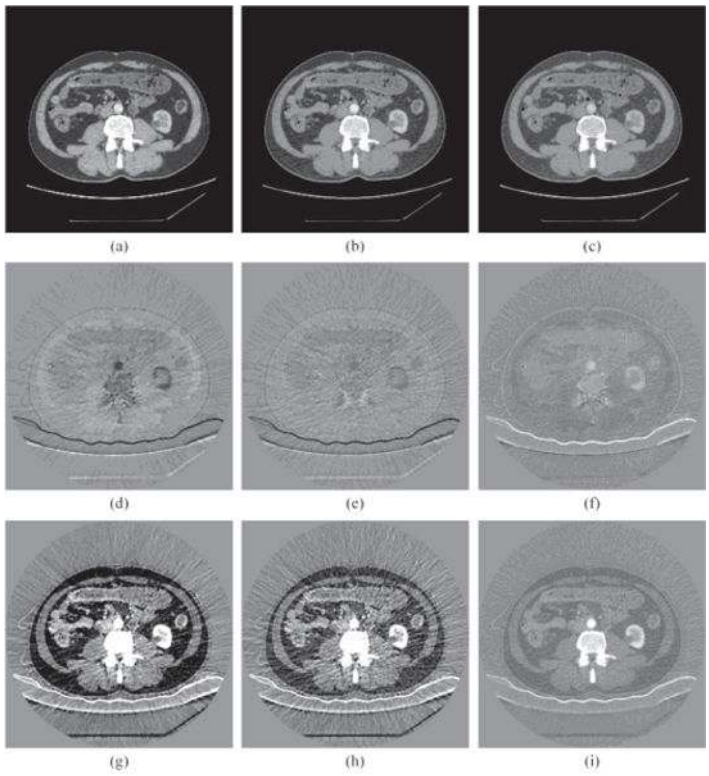

Fig. 5.

Results using the linear mapping function. (a) The 60 keV image estimated from the 100 keV image, (b) the 80 keV image estimated from the 60 keV image, (c) the 100 keV image estimated from the 80 keV image, (d) the difference between the estimated and original 60 keV images, (e) the difference between the estimated and original 80 keV images, (f) the difference between the estimated and original 100 keV images, (g) the difference between the 60 and 100 keV images, (h) the difference between the 80 and 60 keV images, and (i) the difference between the 100 and 80 keV images. The display window for the spectral images and difference images are [845 1295] and [−50 50] HU respectively.

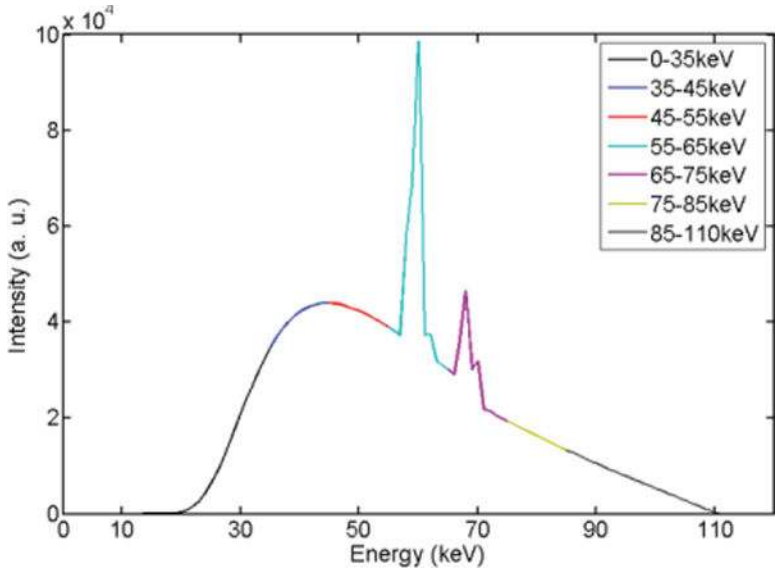

Fig. 6.

X-ray spectrum at 110 kVp which was divide into seven energy bins.

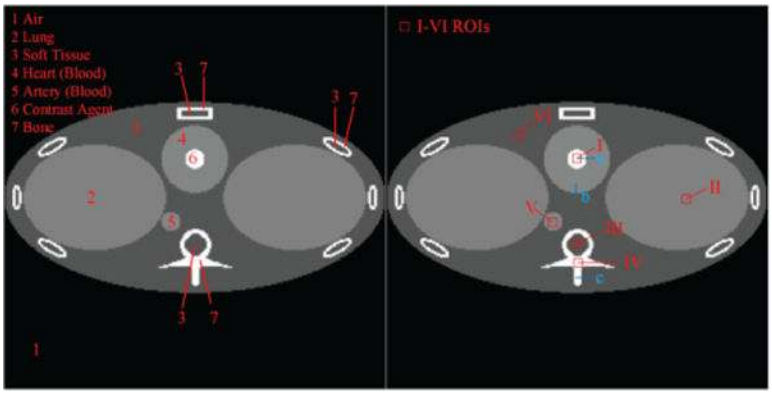

Fig. 7.
FORBILD thorax phantom at 50keV. The display window is [−150 300] HU.

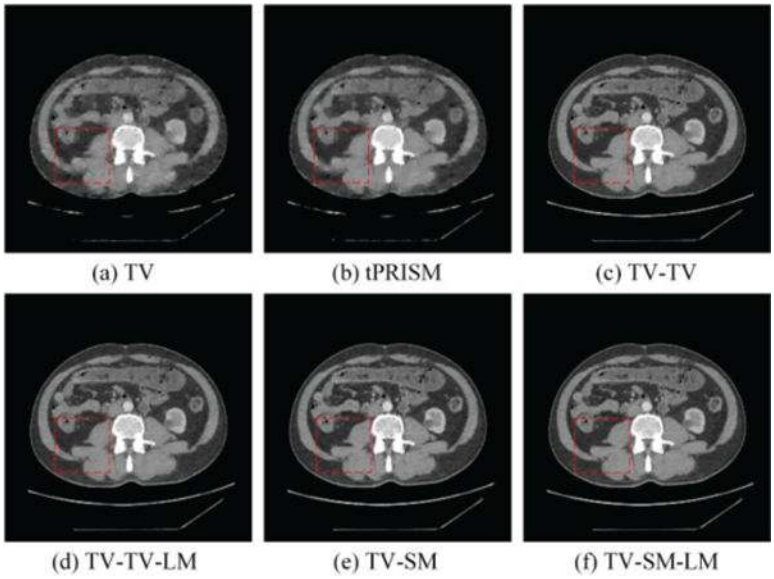

Fig. 8.

Reconstructed 80 keV images using different methods for comparison. (a) TV, (b) tPRISM, (c) TV-TV, (d) TV-TV-LM, (e) TV-SM, and (f) TV-SM-LM images respectively. The display window is [845, 1295] HU.

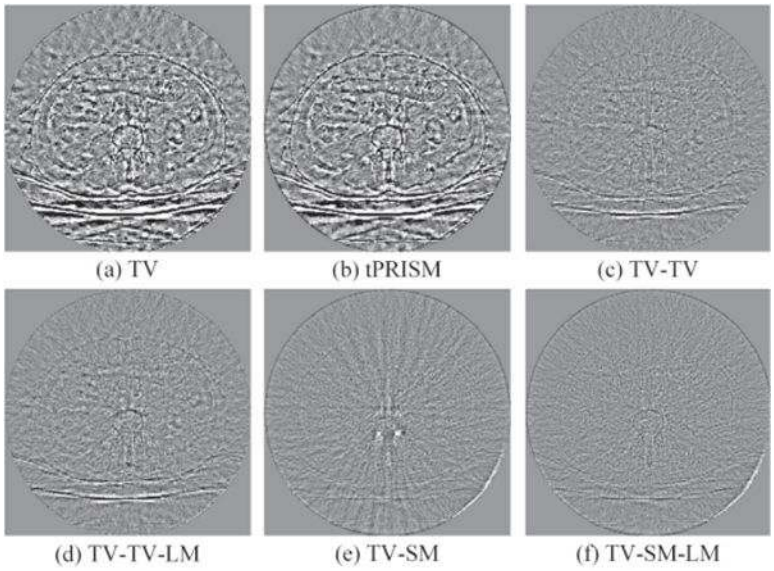

Fig. 9.

Difference images relative to the reference. (a) TV, (b) tPRISM, (c) TV-TV, (d) TV-TV-LM, (e) TV-SM and (f) TV-SM-LM reconstructions in the 80 keV energy bin. The display window is [−50, 50] HU.

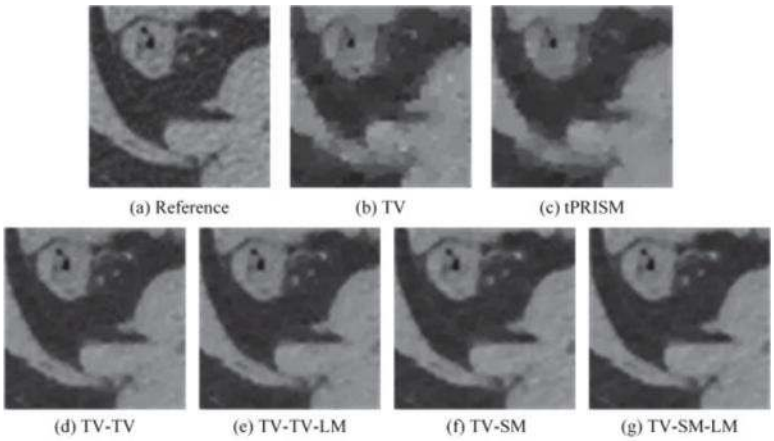

Fig. 10.

Zoomed reference (a) and the images reconstructed using the (b) TV, (c) tPRISM, (d)TV-TV, (e) TV-TV-LM, (f) TV-SM and (g) TV-SM-LM algorithms respectively in the 80 keV energy bin. The display window is [845, 1295] HU.

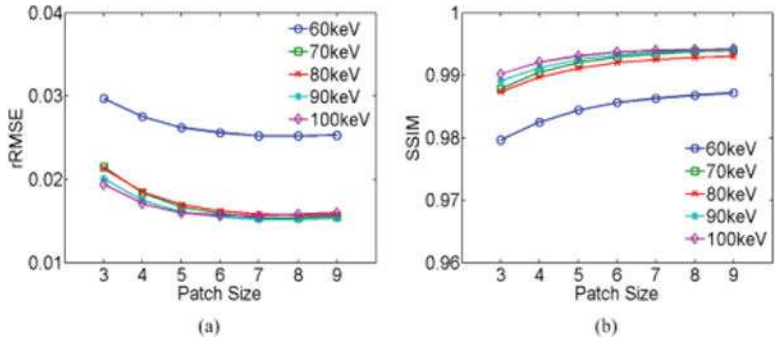

Fig. 11.

Image quality indices with TV-SM-LM with respect to the patch size n_p. The performances of TV-SM-LM are quantified by (a) rRMSE and (b) SSIM values for different patch sizes.

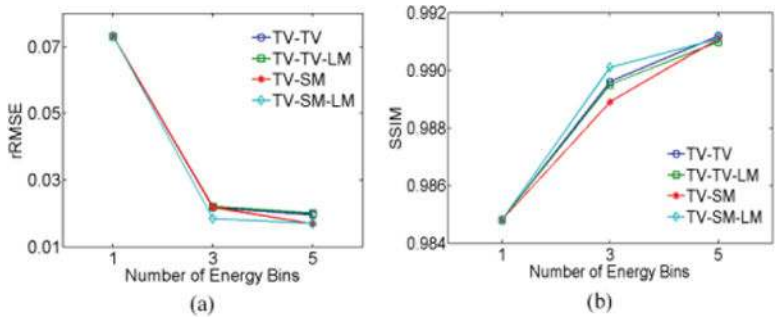

Fig. 12.

Results of TV-TV, TV-TV-LM, TV-SM and TV-SM-LM versus the number of energy bins *J*. The performances of TV-TV, TV-TV-LM, TV-SM and TV-SM-LM are quantified by (a) rRMSE and (b) SSIM values for different numbers of energy bins.

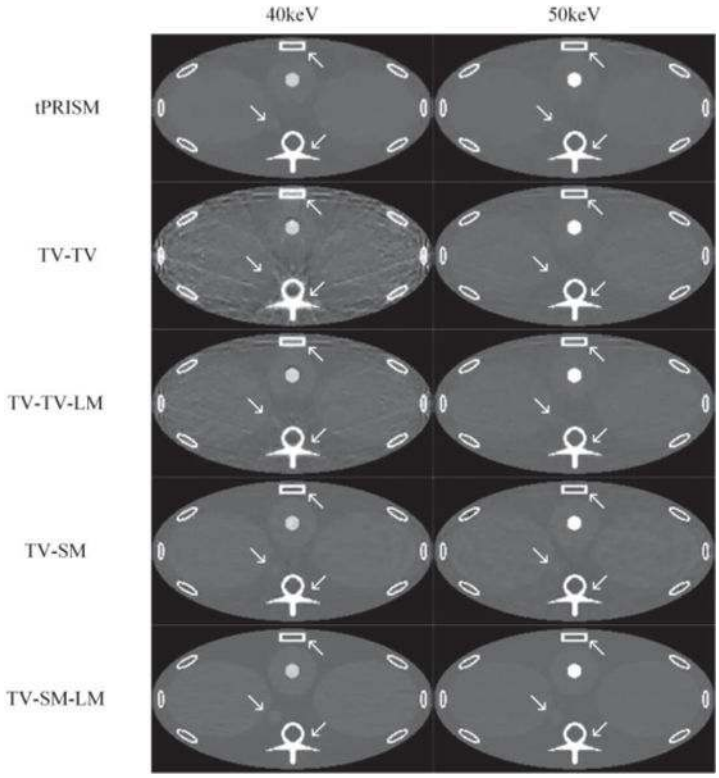

Fig. 13.

Reconstructed 40 and 50 keV images from noisy polychromatic measurements for comparison. The display window is [0, 1500] HU.

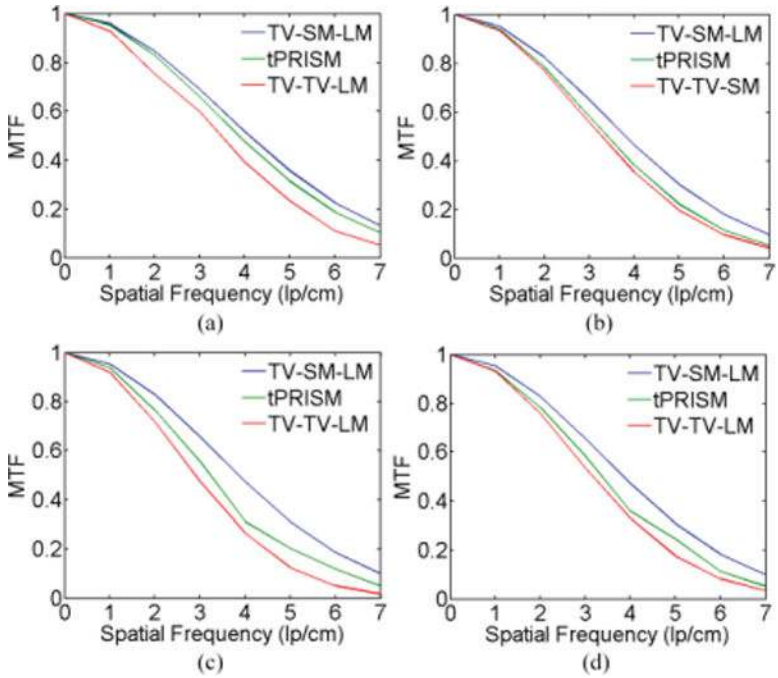

Fig. 14.

MTF curves obtained for different algorithms at (a) 40 keV in high contrast level (line a), (b) 50 keV in high contrast level (line a), (c) 40keV in low contrast level (line b), and (d) 40 keV in low contrast level (line b).

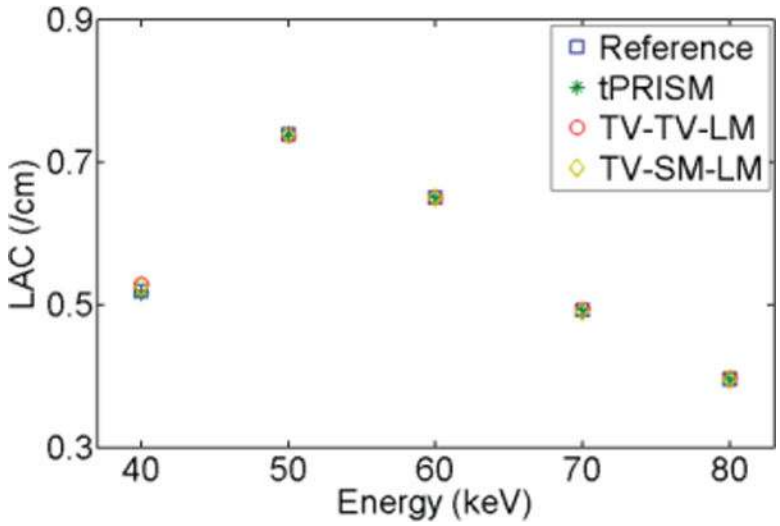

Fig. 15.

Means of linear attenuation coefficients in the region of contrast agent for different energy bins reconstructed by various methods respectively.

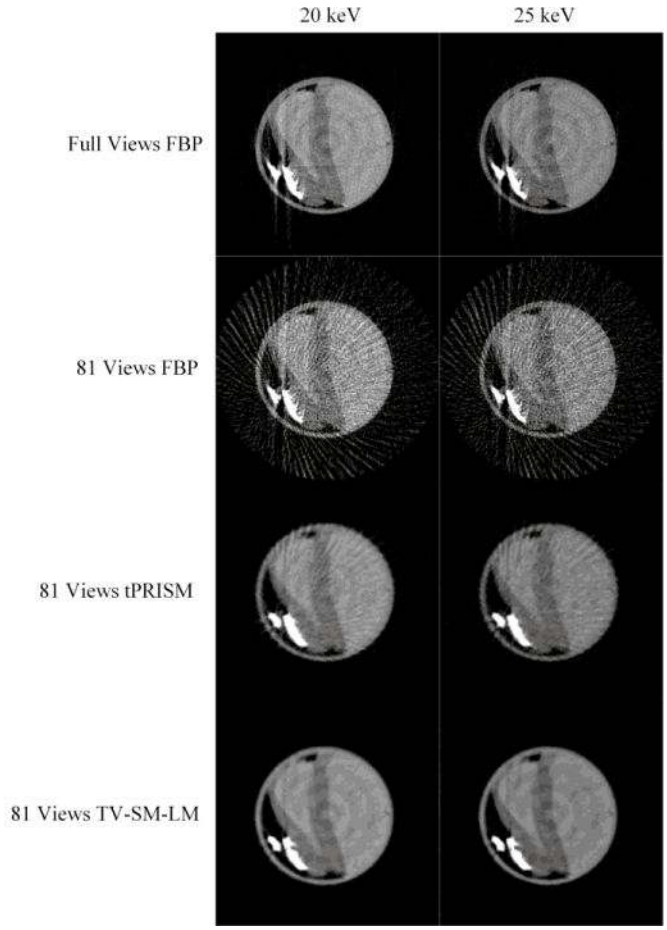

Fig. 16.

Reconstructed images at 20keV and 25 keV respectively for comparison. The display window is [0, 500] HU.

TABLE I

LINEAR COMBINATION COEFFICIENTS OF MATERIAL DECOMPOSITION VIA LEAST SQUARES FITTING

Material	$\mathbf{a_1}$	$\mathbf{a_2}$	**RMSE**
Water	0.000	1.000	0.000
Bone	1.000	0.000	0.000
Adipose Tissue	−0.034	1.011	0.021
Blood	0.005	1.041	0.004
Brain	0.005	1.020	0.004
Breast Tissue	−0.017	1.045	0.011
Eye Lens	−0.013	1.110	0.008
Lung	0.006	1.029	0.004
Muscle	0.004	1.034	0.004
Testes	0.004	1.025	0.003
Soft Tissue	−0.006	1.003	0.008
Iodine	−213.693	132.795	0.023
Gadolinium	298.907	−1.784	0.445
Renal Calculi	−0.443	1.321	0.018

TABLE II

MAIN STEPS FOR TV-SM-LM

Algorithm of TV-SM-LM

Initialization:

Given y_k for k=1,2,…,K, h, λ, α, β, γ, N_{outer}, tol.

$$f_k^0=d_x^0=d_y^0=d_f^0=d_x^0=d_y^0=d_f^0=0.$$

Calculate the linear coefficients for the linear mapping functions $L(\cdot)$.

Main Loop:

while $\|f_k^{i+1}-f_k^i\|_2^2/\|f_k^{i+1}\|_2^2>tol$ and $i < N_{outer}$

Update w_t according to Eq. (12).

$$f_k^{i+1}=(\alpha M_k^T M_k-\beta\Delta+\gamma I)^{-1}(\alpha M_k^T y_k$$
$$\beta(\nabla_x^T d_x^i-\nabla_x^T b_x^i+\nabla_y^T d_y^i-\nabla_y^T b_y^i)+\gamma(d_f^i+\overline{f}_k^{est,i}-b_f^i))$$

$$d_x^{i+1}=\mathrm{shirnk}(\nabla_x f_k^{i+1}+b_x^i,1/\beta)$$

$$d_y^{i+1}=\mathrm{shirnk}(\nabla_y f_k^{i+1}+b_y^i,1/\beta)$$

$$d_f^{i+1}=\gamma\left(\alpha\sum_t w_t R_t^T R_t+\gamma I\right)^{-1}\cdot\left(f_k^{i+1}-\overline{f}_k^{est,i+1}+b_f^i\right)$$

$$b_x^{i+1}=b_x^i+\nabla_x f_k^{i+1}-d_x^{i+1}$$

$$b_y^{i+1}=b_y^i+\nabla_y f_k^{i+1}-d_y^{i+1}$$

$$b_f^{i+1}=b_f^i+(f_k^{i+1}-\overline{f}_k^{est,i+1})-d_y^{i+1}$$

$i=i+1$

end while

TABLE III

rRMSE VALUES ASSOCIATED WITH DIFFERENT ALGORITHMS FOR THE CLINICAL IMAGE

	TV	tPRISM	TV-TV	TV-TV-LM	TV-SM	TV-SM-LM
60keV	0.0730	0.0367	0.0295	0.0271	0.0304	**0.0252**
70keV	0.0745	0.0340	0.0196	0.0190	0.0163	**0.0154**
80keV	0.0733	0.0372	0.0195	0.0200	0.0160	**0.0158**
90keV	0.0677	0.0376	0.0177	0.0188	0.0166	**0.0152**
100keV	0.0683	0.0367	0.0172	0.0188	0.0178	**0.0156**

TABLE IV

SSIM VALUES ASSOCIATED WITH DIFFERENT ALGORITHMS FOR THE CLINICAL IMAGE

	TV	tPRISM	TV-TV	TV-TV-LM	TV-SM	TV-SM-LM
60keV	0.9362	0.9426	0.9819	0.9848	0.9803	**0.9863**
70keV	0.9435	0.9505	0.9915	0.9922	0.9925	**0.9934**
80keV	0.9436	0.9494	0.9912	0.9910	0.9921	**0.9925**
90keV	0.9514	0.9579	0.9934	0.9929	0.9927	**0.9937**
100keV	0.9533	0.9610	**0.9942**	0.9935	0.9924	**0.9940**

TABLE V

rRMSE VALUES ASSOCIATED WITH DIFFERENT ALGORITHMS FOR THE THORAX PHANTOM

	tPRISM	TV-TV	TV-TV-LM	TV-SM	TV-SM-LM
40keV	0.0272	0.1619	0.0826	0.0654	**0.0222**
50keV	0.0347	0.0722	0.0658	0.0613	**0.0377**
60keV	0.0309	0.0569	0.0448	0.0485	**0.0205**
70keV	0.0290	0.0684	0.0388	0.0334	**0.0198**
80keV	0.0277	0.0620	0.0339	0.0271	**0.0201**

TABLE VI

SSIM VALUES ASSOCIATED WITH DIFFERENT ALGORITHMS FOR THE THORAX PHANTOM

	tPRISM	TV-TV	TV-TV-LM	TV-SM	TV-SM-LM
40keV	0.9955	0.9384	0.9699	0.9951	**0.9974**
50keV	0.9942	0.9589	0.9792	0.9927	**0.9977**
60keV	0.9950	0.9633	0.9739	0.9950	**0.9987**
70keV	0.9942	0.9653	0.9751	0.9931	**0.9988**
80keV	0.9951	0.9660	0.9760	0.9956	**0.9987**

IEEE Trans Comput Imaging. Author manuscript; available in PMC 2017 December 01.

TABLE VII

Summary of statistical analysis (mean, SD and *P* value) of ROIs defined within thorax phantom between affected image and that corrected by FBP and affected image and that corrected by TV-TV-LM.

	40keV				50keV			
ROI	**Reference**	**FBP***	**TV-SM-LM***	**P value**	**Reference**	**FBP***	**TV-SM-LM***	**P value**
I	1976	2821±789	1944±31	0.0012	3289	3339±598	3210±57	0.2455
II	1056	1224±535	1057±3	0.1640	1050	1201±556	1048±5	0.0973
III	977	1735±913	975±2	<0.0001	983	1201±1091	986±10	0.2948
IV	4629	5581±984	4631±11	0.0030	3514	2749±1061	3516±8	0.0011
V	1064	1820±878	1074±5	0.0002	1059	1584±874	1062±4	<0.0001
VI	977	1288±768	977±8	0.0002	983	848±599	999±6	<0.0001

*Data are the mean HU values ± standard deviation.